VECTOR: Velocity Based Temperature-field Monitoring with Distributed Acoustic Devices

HAORAN WAN, Nanjing University, China
LEI WANG, Nanjing University, China
TING ZHAO, Nanjing University, China
KE SUN, University of California, San Diego, USA
SHUYU SHI, Nanjing University, China
HAIPENG DAI, Nanjing University, China
GUIHAI CHEN, Nanjing University, China
HAODONG LIU, Huawei, China
WEI WANG, Nanjing University, China

Ambient temperature distribution monitoring is desired in a variety of real-life applications including indoors temperature control and building energy management. Traditional temperature sensors have their limitations in the aspects of single point/item based measurements, slow response time and huge cost for distribution estimation. In this paper, we introduce VECTOR, a temperature-field monitoring system that achieves high temperature sensing accuracy and fast response time using commercial sound playing/recording devices. First, our system uses a distributed ranging algorithm to measure the time-of-flight of multiple sound paths with microsecond resolution. We then propose a dRadon transform algorithm that reconstructs the temperature distribution from the measured speed of sound along different paths. Our experimental results show that we can measure the temperature with an error of 0.25°C from single sound path and reconstruct the temperature distribution at a decimeter-level spatial resolution.

CCS Concepts: • **Human-centered computing → Ubiquitous and mobile computing systems and tools**.

Additional Key Words and Phrases: Temperature monitoring, Acoustic signals, Wireless sensing.

ACM Reference Format:
Haoran Wan, Lei Wang, Ting Zhao, Ke Sun, Shuyu Shi, Haipeng Dai, Guihai Chen, Haodong Liu, and Wei Wang. 2022. VECTOR: Velocity Based Temperature-field Monitoring with Distributed Acoustic Devices. *Proc. ACM Interact. Mob. Wearable Ubiquitous Technol.* 6, 3, Article 144 (September 2022), 28 pages. https://doi.org/10.1145/3550336

1 INTRODUCTION

Ambient temperature monitoring is vital to a variety of ubiquitous computing applications, from warehouse monitoring [1] to building energy management [2] and greenhouse temperature control [3]. With the ever

Authors' addresses: Haoran Wan, wanhr@smail.nju.edu.cn, Nanjing University, Nanjing, Jiangsu, China, 210023; Lei Wang, wang_l@pku.edu.cn, Nanjing University, Nanjing, Jiangsu, China, 210023; Ting Zhao, zhaoting@smail.nju.edu.cn, Nanjing University, Nanjing, Jiangsu, China, 210023; Ke Sun, kesun@eng.ucsd.edu, University of California, San Diego, La Jolla, California, USA, 92093; Shuyu Shi, ssy@nju.edu.cn, Nanjing University, Nanjing, Jiangsu, China, 210023; Haipeng Dai, haipengdai@nju.edu.cn, Nanjing University, Nanjing, Jiangsu, China, 210023; Guihai Chen, gchen@nju.edu.cn, Nanjing University, Nanjing, Jiangsu, China, 210023; Haodong Liu, liuhaodong@huawei.com, Huawei, Shanghai, Shanghai, China, 300060; Wei Wang, ww@nju.edu.cn, Nanjing University, Nanjing, Jiangsu, China, 210023.

2474-9567/2022/9-ART144 $15.00
https://doi.org/10.1145/3550336

increasing user demands, the capability of monitoring the temperature distribution within a given space, *e.g.*, in a room or in a car, becomes important for the next generation HVAC (Heating, Ventilation, and Air Conditioning) systems. Instead of a single temperature reading given by traditional temperature sensing systems, temperature distribution monitoring systems provide fine-grained spatial temperature variation information of the target area. For warehouse monitoring, temperature requirements for food storage are strict and vary for different types of food that are stored in different places of the same warehouse, *e.g.*, 32 ∼ 40°F (0 ∼ 4.4 in Celsius) for refrigerated storage and 50°F (10°C) for dry food storage [4]. For indoor air conditioning, precise temperature monitoring and controlling are vital given that city folk spend 80 ∼ 90% of their time indoors [5, 6]. Different users may have different temperature preferences and improper indoor temperature would cause low productivity and even sickness [7]. Different parts of the same room may also have different heating conditions due to sunlight from windows or room occupation. Moreover, air conditioners and electric fans have accounted for 10% of all global electricity consumption [8]. With precise temperature control, the energy consumption could be reduced by more than 30% while maintaining the thermal comfort for users [9]. As the premise for precise temperature distribution control, the capability of monitoring the temperature of different locations in the same space becomes an important research issue.

Widely used temperature sensors cannot satisfy the demands for temperature distribution monitoring. First, most temperature sensors only measure the temperature at a single location. To reconstruct the temperature distribution, we have to densely deploy temperature sensors over the space. While the cost of temperature sensors are low, the wiring and deployment cost could be far more than the sensor hardware, even for small spaces such as in the car or in a room. Existing works try to infer the ambient temperature distribution using physical model [10] with the assumption that temperature sensor's readings represent the average in a room or a confined space. Such estimations are unreliable and coarse-grained, since our experiments show that the temperature difference can be as large as 3°C within the limited space in a car. While infrared cameras can capture temperature distribution [11], they are still too expensive for environment monitoring applications. Second, most temperature sensors are based on thermistors or thermocouples, which measures the temperature of the sensor's probe instead of the air. Therefore, the material of the sensor need to be heated/cooled when the temperature changes so that these sensors have large response delays. Such extra delays often lead to difficulties in designing a stable fine-grained temperature control algorithm. With ubiquitous mobile devices and wireless signals (acoustic signal and electromagnetic signal including mmWave and Wi-Fi signals) surrounding us, it's natural to come to the idea of reusing these existing devices and signals to conduct temperature distribution estimation. However, most existing works focus on approximating and replacing the traditional temperature sensors with mobile devices [12] or RFID tags [13, 14] and only measure the temperature for single point or item [15].

In this paper, we develop a system called VECTOR, (Velocity based Temperature-field Monitoring), that can reconstruct the temperature distribution with a small number of low-cost ubiquitous acoustic devices. Our design is based on the fact that the speed of sound is physically related to the air temperature along the sound propagation path. Therefore, we can infer the temperature along a given path using the time-of-flight (ToF) measurements of sound signals. As illustrated in Fig. 1(a), a pair of acoustic devices can monitor multiple acoustic paths passing through different regions in a car. Temperature changes on different regions incur different phase variations determined by the ToF along specific segments of the sound paths. Therefore, we can reconstruct the temperature distribution using the different phases changes of these line-of-sight (LoS) paths and reflected paths. In our experiments, VECTOR can measure the temperature along the sound path with an accuracy of 0.25°C by sensing slight changes in the speed of sound, when the distance between two devices is known. Moreover, VECTOR incurs minimal hardware cost, as it can reuse the built-in audio systems that are already widely deployed in indoor environments or in cars. Compared with traditional temperature sensors, the sound-based scheme directly measures the temperature in the air instead of the temperature of the sensor. Therefore, VECTOR can detect human perceivable temperature fluctuations within a few seconds, while the latency of traditional sensor

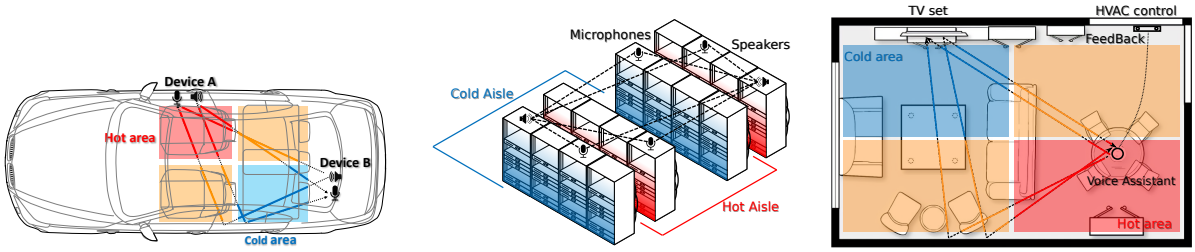

(a) In-car temperature-field reconstruction using sound velocity along multiple paths.

(b) Providing feedback for DC energy management systems.

(c) Smart home/buildings with flexible temperature demands.

Fig. 1. Application scenarios.

is at a scale of tens of seconds. The sensitivity of VECTOR allows next-generation HVAC systems to recognize different types of heat sources and take timely reactions. With an array of distributed acoustic devices, we can reconstruct the temperature distribution with comparable resolution to infrared cameras, as shown in Fig. 7(c).

We face three key technical challenges when developing VECTOR. The first challenge is to precisely measure the ToF of the sound signal along each paths. For a 60 cm path, temperature change of 1°C at room temperature of 25°C yields a 3.02 μs difference in ToF, which is far less than the 20 μs sampling interval of widely used sound sampling frequency of 48 kHz on commercial devices. To achieve precise ToF measurement, we design an Orthogonal Frequency-Division Multiplexing (OFDM) sensing signal that can measure both the coarse-grained cross-correlation estimation and the fine-grained phase estimation. Our coarse-grained correlation scheme measures ToF at the sampling interval level ($20\mu s$), while fine-grained phase estimation achieves sub-microsecond time resolution using the phase of the carrier frequency at 19 kHz. By removing the ambiguity of phase measurement using the coarse-grained correlation results, we can achieve a ToF accuracy of $0.371\mu s$, which is enough to capture temperature change of 0.12°C along a 60 cm path. The second challenge is to reconstruct the temperature distribution using the ToF measurements. Intuitively, traditional Radon transform measures the signal attenuation from multiple angles to reconstruct the image of the object [16] and we can reuse it onto our cause to reconstruct the temperature distribution in the same manner. However, the ToF is reciprocally related to the speed of the sound and the temperature so that our physical model is different to the traditional Radon transform. To address this challenge, we propose the dRandon transform algorithm by transforming the temperature term using Taylor series expansion and use the relative phase changes to reconstruct the temperature distribution. The third challenge is to reconstruct the temperature distribution with limited acoustic devices. In real-world scenarios, we cannot get the acoustic paths in all desired angles with a small number of devices. To address this challenge, we utilize reflected paths to increase the number of phase measurements and train a linear model to reconstruct the temperature distribution as shown in Fig. 1(a).

Our experimental results show that VECTOR can measure the temperature on the LOS path with an error of 0.25°C and reconstruct the temperature distribution with a decimeter-level spatial resolution. By monitoring multiple reflection paths in a car, VECTOR can measure distinct temperatures of all four seats with an average error of 0.44°C using only one pair of devices.

2 MOTIVATION AND APPLICATION SCENARIOS

2.1 Motivation

The motivation of using acoustic signal as the medium of temperature sensing is twofold:

- **Performance:** The key performance advantages of acoustic temperature sensing are in its low latency and long-range measurement capabilities. First, the speed of acoustic signal is physically determined by the air temperature, which incurs almost no delay. In many scenarios, air temperature could change quickly due to air conditioning, sunshine, or workload of servers in data centers, where such change could be captured by acoustic sensing. In contrast, traditional temperature sensors measure the temperature of their sensor probes, which could be different from the air temperature due to thermal conduction process. Second, with acoustic sensing, we can measure the average temperature along a long distance and use distributed devices to cover a large indoor area. Traditional sensors can only capture the temperature of a given point, and they are often placed on the wall or near the roof that are far way from the target region.
- **Cost:** Sound devices are ubiquitous in daily life, *e.g.*, voice assistants in home and car, speakers and microphones for electronic devices, so that acoustic sensing can reach the region of interest (living or working area) with no extra cost. Deploying traditional temperature sensors to provide acceptable coverage of the target regions may incur extra cost and inconvenience for daily activities. Therefore, our acoustic sensing method provides a low-cost solution to upgrade the temperature measurement performance.

2.2 Application Scenarios

With the advantages of line coverage, low latency, and low cost, VECTOR can enable the following new application scenarios:

- **In-car temperature sensor:** In future smart vehicles, the electronics would make up 35% of a car's cost [17], which also make the wiring harness replacement/repair labor and cost skyrocket [18]. VECTOR can reuse the built-in microphone and speaker in the car to provide fine-grained temperature readings, as shown in Fig. 1(a). By measuring temperatures of individual seats and react to thermal condition changes with low-latency, VECTOR can improve the thermal comfort of occupancy with no extra hardware cost. Furthermore, replacing traditional sensors with VECTOR by existing acoustic hardware can largely reduce the cost for both manufacturers and customers.
- **Front-end of data center thermal management system:** Data Centers (DCs) consume oceans of energy, *e.g.*, in 2014, DCs in U.S. consumed 1.8% of country's electricity consumption and 40% of the energy is used for temperature management [19]. In Singapore, this ratio was 7% due to the tropical climate [20]. There are a series of research works in both academia [21–23] and industry [24] in designing the HAVC control systems in DCs using temperature sensors as the feedback signal. As shown in Fig. 1(b), VECTOR can provide the air temperature for multiple hot/cold aisles and racks with lower feedback latency and higher granularity compared with traditional sensors. Generally, feedback with lower latency can reduce the response time for a control system [25] and given the huge energy consumption of DCs, shorter response time means saving more energy.
- **Cooperation with smart home/buildings:** Thermal design of smart home/buildings aims at providing thermal demand flexibility with least energy consumption [26]. Heating power loss coefficient (HPLC) are used to evaluate the thermal efficient of houses [27] and VECTOR can detect the heating sources without connection to the heating device and provide the heating periods data required by HPLC [26, 27]. In addition, VECTOR can be easily integrated with existing thermal efficiency systems such as Google Nest Thermostats [28]. Another important research issue for smart buildings is demand flexibility for thermal comfort [29–31], where VECTOR can provide temperature management systems with the temperature distribution using a small number of existing acoustic devices, as shown in Fig. 1(c).

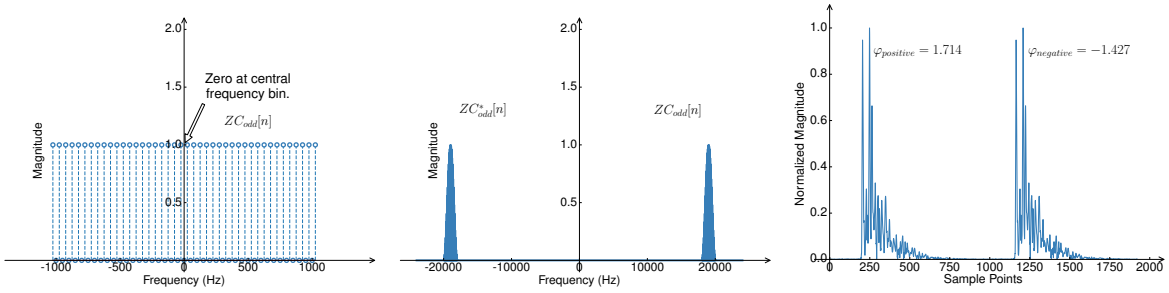

(a) Baseband signal for odd subcarriers in frequency domain.

(b) Modulated odd subcarriers in frequency domain.

(c) CIR of odd subcarriers with rich environmental multipaths.

Fig. 2. Key intermediate steps of signal processing.

3 SIGNAL DESIGN

In the section, we first introduce the physical relationship between temperature and the speed of sound. We then design an OFDM sound signal to accurately measure the ToF along a sound path to derive the temperature.

3.1 Background

The speed of sound in the air depends on environmental variables such as temperature, humidity, and air pressure. Within the normal room temperature range, the speed of sound can be approximated as

$$c = 331.3 + 0.606 \times T \qquad m/s, \tag{1}$$

where the temperature T is in degrees Celsius (°C). While there are better approximations that relate the speed of sound to both temperature and air pressure [32], we use Eq. (1) as it is accurate enough for our system.

We observe that the speed of sound increases by around 0.2% when the air temperature raises by one degree Celsius at room temperature. As an example, for two devices that are separated by a distance of 60 cm, the ToF measurement will decrease by a small amount of 3.02 μs based on Eq. (1). Under the widely supported sampling rate of 48 kHz for sound playing/recording, the interval between consecutive samples is 20.8μs, which is far greater than the small change in ToF. Therefore, traditional correlation-based ranging schemes cannot reliably detect such small changes in ToF, which is less than the sampling interval. To this end, we use an OFDM modulated signal to capture both the coarse-grained cross-correlation measure and the fine-grained phase measurement to detect microsecond-level changes in ToF.

Phase-based ToF measurement provides high-resolution and reliable ToF results. The phase change for a specific path p, ϕ_p, is related to the speed of sound by $\phi_p = -2\pi d_p f_c / c$, where d_p is the length of the path and f_c is the carrier frequency of the signal. In the following discussion, we use the carrier frequency of $f_c = 19\ kHz$ if not specified. For two devices that are separated by a distance of 60 cm, the phase change will decrease by an amount of 0.360 in radian when the temperature raises by one degree at room temperature. Such phase increase can be reliably measured using OFDM signals [33]. However, as phase changes are limited in the range of $0 \sim 2\pi$, it cannot determine whether the phase changes by 0.5π or 2.5π. We use coarse-grained cross-correlation results to resolve the ambiguity in phase measurements. As a phase change of 2π at 19 kHz carrier is equivalent to 52.6 μs in ToF, we can use the cross-correlation result that has a resolution of 20.8 μs to determine how many 2π the phase has been changed. Therefore, we design an OFDM signal that can measure both the phase and the cross-correlation offset at the same time.

3.2 Signal Design

Low-end commercial acoustic devices have severe clock drifting problems so that the reference time between devices could change by more than $50\mu s$ per second [34]. Such clock drifting leads to errors in ToF measurements that are far larger than the ToF changes due to temperature difference. Traditional acoustic sensing applications require a calibration process for each session, *i.e.*, whenever the sound play/recording restarts, to reduce the clock drift [33, 35, 36]. In stead of asking user to calibrate the devices for each session, we adopt an OFDM full-duplex signal design to remove the transmitting and receiving delay introduced by low-end commercial devices. When we have two devices, we ask both devices to transmit and receive sound signals at the same time to perform a ToF measurement session. Devices can turn-off between sessions to save energy. Our experiments show that our scheme can output the correct ToF within 0.5 seconds after both devices start sound transmission. Therefore, our system can work with low-duty cycles in stable environments, *e.g.*, turn on for only 0.5 seconds in every minute.

We choose the Zadoff Chu (ZC) sequence [37] as our baseband signal, which has an ideal cross-correlation property [38]. The baseband ZC sequence with a length of N_{zc} is:

$$zc[n] = exp\left(-j\frac{\pi un(n+1+2q)}{N_{zc}}\right), \tag{2}$$

where $0 \leq n < N_{zc}$, q is a constant integer and j is the imaginary unit, *i.e.*, $j^2 = -1$. N_{zc} is the length of sequence, which determines the bandwidth in the final modulated signal. For example, if we set N_{zc} to 653 and the frame length to 4800 sample points, the bandwidth of the modulated signal would be $653/4800 \times 48 = 6.53\ kHz$ under 48 kHz sampling rate. The parameter u determines the correlation property and it should be coprime to N_{zc}, *i.e.*, $gcd(N_{zc}, u) = 1$.

We use Orthogonal Frequency-Division Multiple Access (OFDMA) scheme to allow both devices to transmit at the same time and in the same frequency band. Our OFDMA scheme allocates odd subcarriers for one device and even subcarriers for the other to avoid collision. We also choose two different values of u when generating baseband ZC sequence to further reduce the interference between the two devices. Specifically, the frequency domain baseband signals for the two devices are:

$$ZC_{odd}[n] = fft\_shift\left(FFT\left(exp\left(-j\frac{\pi u_{odd} n(n+1+2q)}{N_{zc}}\right)\right)\right) \times g[n], \tag{3}$$

$$ZC_{even}[n] = fft\_shift\left(FFT\left(exp\left(-j\frac{\pi u_{even} n(n+1+2q)}{N_{zc}}\right)\right)\right) \times g[n+1], \tag{4}$$

where $fft\_shift(\cdot)$ is to switch the order of the sequence's first half and the second half in frequency domain to place the zero-frequency point at the center of the sequence for the following modulation process. We set $g[n] = \frac{1}{2}(1-(-1)^{n+1})$ to pick out odd/even subcarriers. Note that the odd or even subcarriers are relative to the central subcarrier (or the subcarrier corresponding to zero-frequency in baseband) instead of the start of the sequence. Fig. 2(a) shows a sample of $ZC_{odd}[n]$ baseband signal with a 2 kHz bandwidth in the frequency domain. As the rectangle window in the frequency domain will cause severe side-lobe (from *sinc* function) in final time domain Channel Impulse Response (CIR), we add a Hanning window to smooth it (shown in Fig. 2(b)).

3.3 Signal Modulation

With the baseband signal generated, we move the sequence to carrier frequency f_c with OFDM modulation before transmitting. To transform the modulated signal to a real signal, we set the negative frequency of the signal to be the conjugate counterpart of the positive frequency parts. This modulation process is shown in Algorithm 1 and we use $ZC_{baseband}$ to denote both ZC_{odd} and ZC_{even} who share the same modulation process. Since the two

signals occupy separate subcarriers in the frequency domain, they can be transmitted simultaneously. Fig. 2(b) shows the modulated signal in the frequency domain.

Algorithm 1: Transmitting signal generation

Result: The modulated sequence $zc_T[n]$ with a length of L and a carrier frequency of f_c.

1 Generate frequency domain baseband signal $ZC_{baseband}$ from Eq. (3) and (4) with a length of N_{zc}.
2 Multiply $ZC_{baseband}$ with a Hanning window with length N_{zc}.
3 Generate a all zero sequence $\widehat{ZC}[n]$ with a length of L.
4 $\widehat{ZC}[\frac{f_c L}{f_s} - \frac{(N_{zc}-1)}{2} : \frac{f_c L}{f_s} + \frac{(N_{zc}-1)}{2}] \Leftarrow ZC_{baseband}[n]$.
5 $\widehat{ZC}[L-1 : L/2+1] \Leftarrow \widehat{ZC}^{*}[1 : L/2-1]$.
6 Perform IFFT on $\widehat{ZC}$ to the time domain $zc_T[n]$.

3.4 Signal Demodulation and ToF Acquisition

On both receiving ends, the received signal with P paths can be modeled as:

$$zc_R[n] = \sum_{i=1}^{P} A_i e^{j\phi_i} zc_T\left[n - \frac{\tau_i}{f_s}\right], \tag{5}$$

where $zc_R[n]$ is received signal, A_i is attenuation coefficient for path i, $\phi_i = -2\pi\tau_i f_c$ is the phase shift caused by the propagation of path i and τ_i is the ToF of path i. To get the absolute phase shift for a given path, we first perform FFT on the received signal and extract the ZC baseband sequence directly from the received signal. Then we perform cross-correlation with the conjugate transform of original baseband $ZC_{odd}[n]$ and $ZC_{even}[n]$ to get the baseband CIR. We use zero-padding on the baseband CIR to expand the length and increase the range resolution brought by sample index, *e.g.*if we pad the baseband to the length 4× the original frame length, the range difference between each sampling point is $1/48000/4 \approx 5.2\ \mu s$.

To acquire the accurate ToF changes for each path, we combine the index of the cross-correlation peak and the phase of the peak. In the ideal case and without zero-padding, the coarse-grained peak position is expressed as the integer part of $\tau_i f_s$, $round\ (\tau_i f_s)$, and the fine-grained phase of the peak is expressed as $mod(-2\pi\tau_i f_c, 2\pi)$, which is between 0 and 2π. We can calculate the absolute phase $\phi_i = -2\pi\tau_i f_c$, which considers whole turns of 2π in phase, by combining these two measurements. However, there are inevitable unknown delays for the transmitting and receiving process in low-end commercial devices. Most existing works require user to put devices on a known position to calibrate and calculate the relative distance [33, 35]. To allow self-calibration without user intervention, we choose to cancel the unknown delays by obtaining reciprocal measurements from both devices. For example, when device A receives signal from device B and the phase shift is $\phi_{BA} = -2\pi(\tau_{BA} + \tau_{AR} + \tau_{BT})f_c$, where τ_{BA} is the signal propagation delay that we wish to measure, τ_{AR} is the receiving delay for device A and τ_{BT} is the transmitting delay for device B. Similarly, we have $\phi_{AA} = -2\pi(\tau_{AA} + \tau_{AR} + \tau_{AT})f_c$ when device A receive its own signal. Device B can also perform two measurements of $\phi_{AB} = -2\pi(\tau_{AB} + \tau_{BR} + \tau_{AT})f_c$ and $\phi_{BB} = -2\pi(\tau_{BB} + \tau_{BR} + \tau_{BT})f_c$. Therefore, we can use $\phi_{AA} + \phi_{BB} - \phi_{AB} - \phi_{BA} = -2\pi(\tau_{AA} + \tau_{BB} - \tau_{AB} - \tau_{BA})f_c$ to cancel the unknown transmitting and receiving delays [39]. We can further assume the distances between the speaker and microphone of same device are fixed so that τ_{AA} and τ_{BB} are known in advance. Therefore, we can measure the ToF by:

$$\tau_{AB} + \tau_{BA} = \left(\tau_{AA} + \tau_{BB} + \frac{\phi_{AA} + \phi_{BB} - \phi_{AB} - \phi_{BA}}{2\pi f_c}\right). \tag{6}$$

If the environment is homogeneous in temperature, using the sum of τ_{AB} and τ_{BA} increases the temperature sensitivity of the system, because the same temperature changes will cause larger ToF changes in longer distance. If the environment is not homogeneous in temperature, paths passing along different temperature regions can help us to reconstruct the temperature distribution discussed in Section 5.

Since we only use half of the baseband frequency bins for each transmitter, the final CIR will have two repeated peaks, as shown in Fig. 2(c). For the device using the even subcarriers, the DC component is not zero and the two peaks are completely the same in both phase and amplitude so that we can use either part for position and phase measurement. For the device using odd subcarriers, the DC component is zero, so the phase for the first peak and the second peak has a phase difference of π. To find the right peak, the device using odd subcarriers first transmits several OFDM frames with full bandwidth to estimate the right delay which, according to our observation, only incurs hundreds of millisecond delay before returning the right temperature result. And the detailed demodulation process is shown in Algorithm 2 and the essential steps of whole signal process is shown in Fig. 2.

Algorithm 2: Received signal demodulation

Result: The interpolated time-domain $cir[n]$.

1 Perform FFT on $zc_R[n]$ to get $ZC_R[n]$.

2 $CIR_{baseband}[n] \Leftarrow ZC_R[\frac{f_c L}{f_s} - \frac{(N_{zc}-1)}{2} : \frac{f_c L}{f_s} + \frac{(N_{zc}-1)}{2}] \times ZC^*_{baseband}[n]$.

3 Generate an all-zero sequence $CIR[n]$ with length $N \times L$.

4 $CIR[\frac{NL}{2} - \frac{N_{zc}-1}{2} : \frac{NL}{2} + \frac{N_{zc}-1}{2}] \Leftarrow CIR_{baseband}[n]$.

5 $CIR[n] \Leftarrow fft\_shift\,(CIR[n])$

6 Perform IFFT on $CIR[n]$ to the time domain $cir[n]$.

3.5 Engineering Details and Discussions

For implementation in real acoustic devices, there are some details and discussions need mentioning:

- **Streaming mode.** We use the streaming control mode for audio playback and recording. The data is periodically put into/get from the playing/recording buffers, which means the recording and playback delays stay the same after the stream starts. Switching from full sequence to odd sequence will not change these delays during one measurement session. For each temperature measurement session, we restart the playback/recording, which introduces unknown delays. However, such delays can be canceled using Eq. (6) so that our ToF results are consistent across different sessions.
- **Influence of multipath.** Due to the limited bandwidth of commercial acoustic devices, the correlation peaks corresponding to paths with close ToF (less than 30 cm in distance) will merge together to form a new peak. In this condition, we cannot distinguish neither peaks' index and phase. Wider bandwidth and longer frame length can reach a higher path resolution and further mitigate this impact. There are also solutions to separate the merged paths with deep learning methods, *e.g.*, using Neural Network to get the right peak location and distance measurement [40, 41]. However, both attempts still cannot separate all the echoes. As we utilize multiple paths to perform measurement, we choose to ignore paths that are interfered by nearby multipath and only use those clean paths to reduce the complexity of our system.
- **Clock drifts.** Different devices with separate clocks will experience clock drifts between each others. The offset will be added in the unknown transmitting and receiving delays which can be canceled along with the delays. Our experiment in Section 6.2 shows that our system can stably measure ToF with drifts less than 0.5 μs for 8 hours.

- **Influence of noise and audibility.** Normal noise from indoor environments occupies different frequency band with our system, so the noise will barely affect our system's performance. And our signal is working on $17 \sim 21\ kHz$ which is insensitive for most of people and will not affect the daily activities.
- **Blocked LOS path.** The LOS path could be blocked in certain extreme cases. We can use paths other than LOS path if the other paths are stable enough, *e.g.*reflection from a nearby wall. The length of the non-LOS path can be estimated with one extra input of temperature and it's an one-time calibration, see details in Section 5.

3.6 Sound-based Temperature Sensing

We use a basic two-device setup to illustrate the fundamentals of sound-based temperature sensing. In this scenario, we separate two devices by a fixed known distance and measure the ToF, *i.e.*, $\tau_{AB} + \tau_{BA}$ in Eq. (6), to derive the temperature. The number of full wave cycles can be determined by the coarse-grained cross-correlation and the decimal part of the cycles can be determined by the fine-grained phase measurement. The wavelength λ_c can be derived by dividing the known distance by the number of wave cycles. We can then calculate the speed of sound by $c = f_c\lambda_c$ and use Eq. (1) to get the temperature. Note that the distance between devices can either be measured in advance, or determined after deployment by calibrating the ToF under a known temperature.

Sound-based temperature sensing is more sensitive than traditional temperature sensors such as thermistors or thermocouples. Acoustic sensing directly measures the temperature of the air, while traditional sensors measure the temperature of the probe that needs to be heated or cooled by surrounding air when the air temperature changes. To evaluate the key features of sound-based temperature sensing, we perform an experiment in a room with controlled temperature changes. Fig. 3 shows the measurements of VECTOR and a traditional Bosch BME280 temperature sensor [42] within a period of two hours. We turned on the air conditioner to heat the room at $t = 500$ seconds, turned it off and opened the window at 2760 seconds, and closed the window at 4270 seconds. Note that we carefully avoided direct air flows towards the sound path in these experiments so that these temperature fluctuations are not caused by air flows. We have three key observations on the result shown in Fig. 3.

- *For stable environments, the difference between the two temperature measurements is smaller than* $0.5°C$. For example, before we start the air conditioner and after we close the window, the sound-based temperature measurement is stable and very close to the readings of BME280 sensor. Therefore, our system can provide accurate temperature readings that are comparable to commercial sensors.
- *We observe that VECTOR responses to temperature changes much faster than traditional sensors.* This can be seen from the differences in the two temperature curves when we turn on/off the heating. For example, when we stopped heating, the measurement of VECTOR drops by 0.5°C within 5 seconds, while BME280 takes 30 seconds to detect the same temperature change. The output of sound-based sensing agrees with human perceptions, since human beings could notice temperature change caused by such events within seconds. The low latency feedback provided by VECTOR could potentially improve the performance of control algorithms in HVAC systems. We further study this phenomenon with detailed experiments in Section 6.6.
- *When the temperature is unstable, VECTOR observes larger short-term variance in the measurements.* For example, when the air conditioner is on or the window is opening, the sound-based measurements have higher fluctuation than the BME280 sensor's readings as shown in Fig. 3. This phenomenon is consistent with our daily experience. When the air conditioner is on, human can perceive the fluctuation of temperatures due to the cool/warm air from the air-conditioner, which is quite different to natural stable environments. However, traditional sensors only perceive smooth temperature changes as shown by Fig. 3. We can leverage

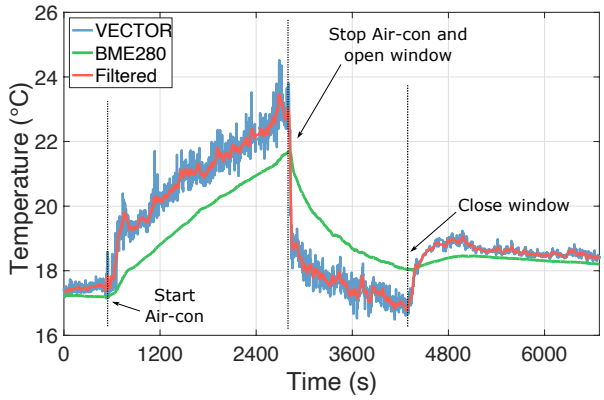

Fig. 3. Preliminary experiment of temperature sensing.

this new capability provided by VECTOR to capture human perceived-temperature for better thermal comfort experience, or to identify the heating source as discussed in Section 6.6.

In our extensive experiments, we also observe that when traditional temperature sensors are exposed to the radiation heating source closely ($30 \sim 50cm$) or sunlight, the temperature reading will exhibit a large mismatch with the air temperature felt by human. For example, the measured ground temperature could be much higher than air temperature in summer. This might be caused by the different thermal transmission types, *e.g.*, radiation in air and heat conduction in the solid sensor probe. If we want to get the air temperature in these scenarios, the sound-based temperature sensing is much more reliable than the probe-based temperature sensing.

4 TEMPERATURE DISTRIBUTION RECONSTRUCTION

As stated in the previous sections, the estimation of air temperature distribution is quite important in many practical scenarios. However, as far as we know, there are few works to measure the actual air temperature distribution. Based on our preliminary experiments of sound-based temperature sensing, we can extend the single path temperature measurements to temperature distribution estimation, using the fact that we are actually measuring the temperature's harmonic mean along the propagation path. In this section, we first introduce the problem of estimating the air temperature distribution and propose a dRadon transform algorithm to solve this problem.

4.1 Problem Statements

We consider the temperature distribution estimation problem in the 2-D scenario. Suppose that there is a target area where each point (x, y) has a temperature of $T(x, y)$, where x and y are Cartesian coordinates. Hence, based on the Eq. (1), the sound speed at the point (x, y) is

$$v(x, y) = v_0 + 0.606(T(x, y) - T_0), \tag{7}$$

where v_0 is the sound speed at a reference temperature T_0, *e.g.*, 0°C.

In our system, we can measure the ToF τ along the given path using cross-correlation and signal phases. For a path L that passes through different points in the target area, the ToF along the path is a line integral:

$$\tau^L = \int_L \frac{\mathrm{d}l}{v(x, y)} = \int_L \frac{1}{v_0} \frac{1}{1 + \frac{0.606(T(x,y)-T_0)}{v_0}} \mathrm{d}l, \tag{8}$$

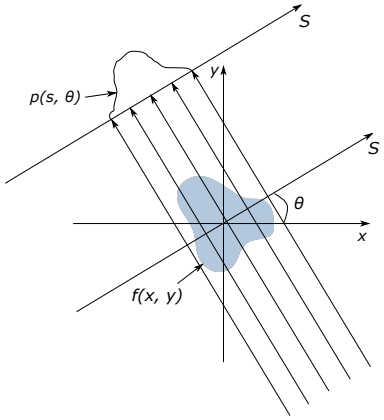

Fig. 4. Basic Radon Transform scenario.

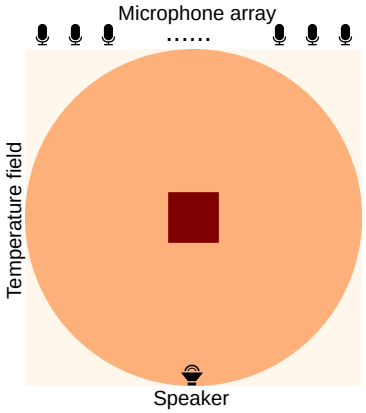

Fig. 5. Simulation setting.

where the differential element $\mathrm{d}l$ is along the signal propagation path L. Therefore, we need to infer the temperature distribution $T(x, y)$ using the ToF along different paths L_i. At first glance, this problem is quite similar to the medical imaging problem tackled with Radon transform. However, traditional Radon transform cannot be directly applied to our problem.

4.2 Background of Radon Transform

Radon Transform is a widely used technology on medical image reconstruction [16]. The basic principle of imaging with radon transform is collecting the projection data $p(s,\ \theta)$ at different locations s on the detector from different angles θ and use back-projection algorithm to transform the data from $(s,\ \theta)$ plane into the $(x,\ y)$ plane. We briefly introduce parallel-beam scenario and demonstrate the difficulties of directly applying Radon Transform.

As shown in Fig. 4, if the target object has a density function of $f(x,\ y)$, we project parallel beam at a given angle θ with different s onto the object. At the detector side, the projection (ray sum/line integral) function can be expressed as

$$p(s, \theta) = \int_L f(x, y)\, \mathrm{d}l, \tag{9}$$

where L is the projection line expressed as $L = x\cos\theta + y\sin\theta - s$ and the s axis is along the detector, as illustrated in Fig. 4. We repeat the process in every angle θ and collect the integral result $p(s, \theta)$, which is usually called sinogram, for every position on the detector. In the back-projection process, the $p(s, \theta)$ is transferred into the Cartesian coordinate (x, y) or polar coordinate (r, ϕ) with Fourier Transform [16].

While the Radon Transform has a similar form as our problem (Equation (8) and (9) if we make $f(x, y) = 1/v(x, y)$), directly applying the Radon Transform cannot reliably reconstruct the temperature field. We use a simulation to illustrate the difficulties in applying Random Transform for our problem. Fig. 5 shows the simulation setting, where we use a speaker as the signal source and 20 microphones as the detectors. We calculate the ToF result τ at every microphone and for different angle θ in the simulation. The simulated temperature field has three parts: the dark red square in the center is hot area with temperature 50°C, the temperature in the circle with light red area is 20°C and the white area out of the target area has 0°C temperature.

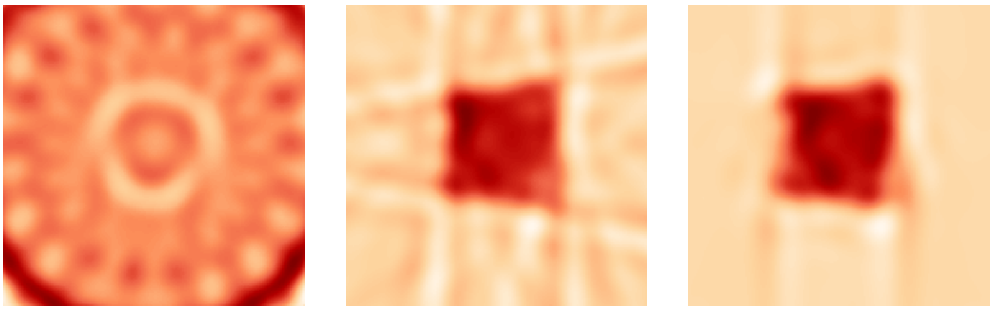

(a) Perform back-projection on ToF directly and take the reciprocal of result.

(b) Result after scanning the image for 18 times.

(c) Result after interpolation on the limited scan sinogram.

Fig. 6. Difficulties in directly using Radon Transform.

- **The projection function is mismatched.** Radon Transform assumes the density/distribution of the object accumulate along the projection. However, we can only measure the ToF that has an integral form of $\tau = \int_L \frac{dl}{v(x,y)}$. The object function $v(x, y)$ is on the denominator and a direct estimation of $f(x, y) = 1/v(x, y)$ is infeasible due to the non-linearity of $f(x, y)$. Fig. 6(a) shows the simulation result when we directly estimate $f(x, y) = 1/v(x, y)$ (perform back-projection on the ToF measurements τ) and then take the reciprocal of the result. The distribution information is completely lost in this case.
- **We can only perform the scan on limited angles.** We use a limited number of acoustic devices and can only rotate the device for a limited discrete set of angles in our scenario. The limited angle resolution reduces the accuracy of distribution estimation. Fig. 6(b) shows the simulation result where we measure the ToF for 18 different angels and reconstruct with dRadon transform, which has phantom lines in the result. Therefore, we need to perform interpolation on the sinogram to improve the accuracy, as shown in Fig. 6(c).

4.3 dRadon Transform Algorithm

We design the dRadon transform algorithm based on traditional Radon transform to reconstruct the temperature distribution.

4.3.1 Taylor Series Approximation. We leverage Taylor series to covert the line integral into a linear function of the temperature. With the Taylor geometric series $\frac{1}{1+x} = \sum_{i=0}^{\infty}(-x)^i$, we can replace the second fraction term in Eq. (8) with:

$$1/\left(1 + \frac{0.606(T(x,y) - T_0)}{v_0}\right) = \sum_{i=0}^{\infty}\left(-\frac{0.606(T(x,y) - T_0)}{v_0}\right)^i. \tag{10}$$

Within the range of room temperature, the temperature is not deviated from T_0 by a large value. Thus, the ratio of speed change, $(0.606(T(x, y) - T_0))/v_0$, is small, since v_0 is around 340 m/s and $0.606(T(x, y) - T_0)$ is often under 10 m/s for indoor air temperature. So, we can ignore higher order terms in the Taylor series and get:

$$\tau^L \approx \int_L \frac{1}{v_0}\left(1 - \frac{0.606(T(x,y) - T_0)}{v_0}\right) \mathrm{d}l. \tag{11}$$

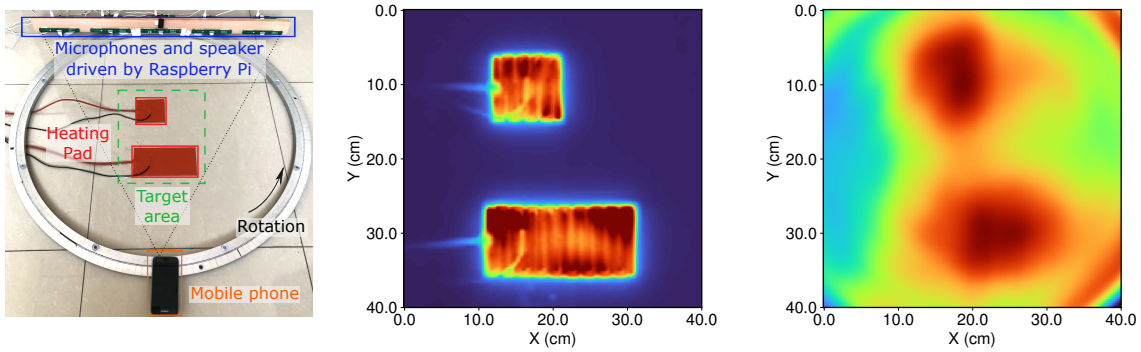

(a) Experimental equipment for dRadon Transform.

(b) Infrared temperature imaging result.

(c) Reconstructed temperature distribution.

Fig. 7. Reconstructing temperature field.

To eliminate the constant term in Eq. (11), we can measure the initial ToF $\tau_0^L = \int_L \mathrm{d}l/v_0$ in a homogeneous temperature flied of T_0. Therefore, we have

$$\begin{aligned} \tau^L - \tau_0^L &= -\int_L \frac{0.606(T(x,y) - T_0)}{v_0^2}\,\mathrm{d}l \\ &= -\frac{0.606}{v_0^2}\int_L T_d(x,y)\,\mathrm{d}l. \end{aligned} \tag{12}$$

We call this differential form of temperature changes as the dRadon transform, which has a similar formulation as the original Radon transform. The dRadon transform directly relates the temperature distribution to the ToF changes that can be captured with multiple microphones in a flat or curve shaped array. Rotating the microphone array by different angles of θ, the microphone array can capture the ToF difference measured on microphone with different values of s on each angle for the dRadon transformation. The reference ToF measurement τ_0^L is an one-time calibration and can be determined once the array is manufactured.

4.3.2 Interpolation and filter on sinogram. Consider the case that we scan on m angles with a microphone array with n elements. After the scan, we can get measurements on $m \times n$ paths and generate a sinogram as $m \times n$ matrix. We first use a moving average filter on it to remove the jitters. We then perform interpolation along the angles axis m to improve the accuracy of the dRadon transform.

4.4 Proof of Concept Experiment

To verify the feasibility of our dRadon algorithm, we perform an experiment on a rotating platform as shown in Fig.7(a). We measure the paths between a mobile phone (Samsung S7) and a distributed microphone array (20 microphones along a line of 95 *cm* using five Raspberry Pis, each with a 4-mic array). We rotate both devices by 2π with a step size of $\pi/18$ to measure the ToF of all paths at different rotation angles. Therefore, we gather ToF on 36×20 paths and we smooth the sinogram with a 3×3 moving average filter and interpolate the *angles* axis from 36 to 360 different angles. We then perform dRadon transformation to reconstruct the temperature field in a 40×40 cm^2 target area at the center of the platform. To generate a stable temperature field, we placed two heating pads with size of 10×10 cm^2 and 10×20 cm^2 in the target area. Fig 7(c) shows that the reconstructed temperature map is similar to the ground truth in Fig. 7(b) obtained through the FLIR infrared camera. Therefore, our ToF measurements are accurate enough to reconstruct the temperature distribution at a decimeter-level resolution.

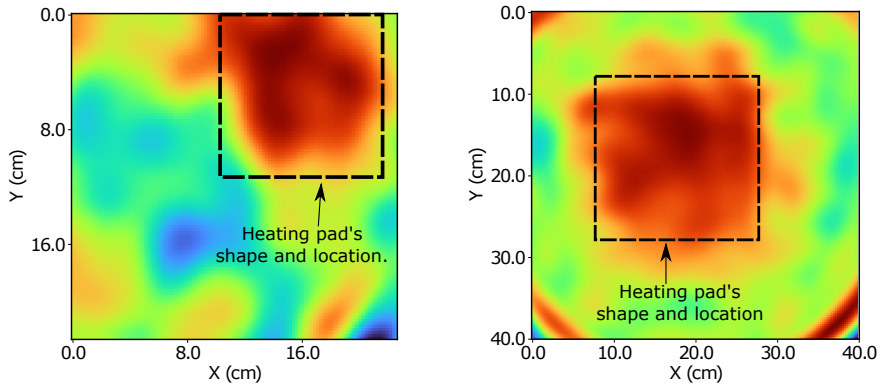

(a) Reconstructed temperature distribution with a 12 microphones array for a 10×10 cm^2 heating pad on the upper right

(b) Reconstructed temperature distribution with a 20 microphones array for a 20×20 cm^2 heating pad in the center.

Fig. 8. Experiments on dRadon algorithm.

We further use arrays with 12 microphones and 20 microphones to evaluate the dRadon algorithm. Fig. 8(a) and 8(b) shows the result of 12-microphone array's reconstruction result for a $10 \times 10 cm^2$ heating pad and 20-microphone array's result for a $20 \times 20 cm^2$ heating pad. Array with smaller number of microphones will reduce the size of the imaging area and the resolution of the reconstruction. For example, with 12-microphones, we can only provide image for the target area with a size of 20×20 cm^2.

4.5 Discussion

- **Ground truth:** In this experiment, we compare the result with the infrared camera images. However, the temperature readings of the infrared camera cannot serve as the ground truth for the air temperature. The infrared camera measures the temperature of the object instead of air, *e.g.*, the surface of the heating pad is around 150°C and the air temperature is just around $30 \sim 40$°C. To the best of our knowledge, there is no COTS device that can measure the air temperature distribution with this high resolution. Therefore, our experiments only show the relative spacial temperature distribution that can be achieved by acoustic sensing.
- **Real-world scenarios:** In most of real-world scenarios, we cannot rotate the acoustic devices to generate multiple LOS paths measurements. With adequate number of microphones and speakers densely deployed on every angle (*e.g.*, separated by 30°), it is possible to perform reconstruction without the rotation process. Such deployment requires a fixed number of devices at desired angles and can fit well in scenarios for a small room or a baby crib. However, even several extra acoustic devices could incur formidable cost when the wiring cost is non-negligible, *e.g.*in a car. Therefore, we design a multipath based solution as discussed in Section 5.
- **Moving objects:** We do not consider the scenario when the hot/cold area moves during the distribution estimating process. If the object movement changes the temperature distribution in the target area, the estimation result could contain large errors because the data in different angles are collected in a time-multiplex way. However, for fixed deployments, the measurement duration could be shorter than the temperature distribution change periods.

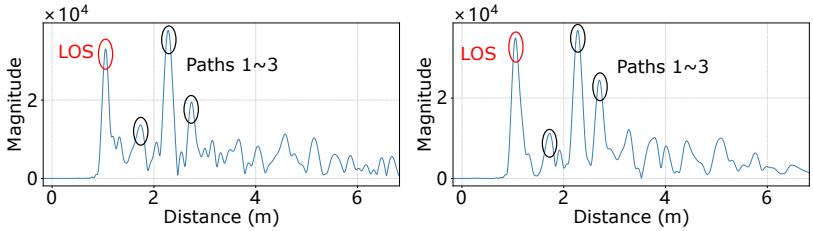

(a) At 5°C (b) At 15°C

Fig. 9. Multipath at different temperatures in the car.

5 RECONSTRUCTION WITH REFLECTIONS

Besides using densely deployed acoustic devices, we can use the multipath effect to get a large number of ToF measurements as illustrated in Fig 1(a).

5.1 Ally with Multipaths

As mentioned in Eq. (5), one frame of CIR contains many paths that are reflection from nearby walls or static objects. Given most of these paths are static, we can leverage their ToF to capture more information about the temperature distribution in the environment. To verify the stability of these multipaths, we place the devices at locations indicated by Fig. 13(c) and near the roof of the car so that the LOS path is not blocked. We use a longer frame length of 7680 samples to increase the unambiguous range to 13.6 meters so that we can capture reflection paths with longer distances. Fig. 9 shows the peaks for the LOS as well as reflected paths observed by Device A in Fig. 1(a) on different days under different temperature. Given an OFDM bandwidth of 4 kHz, our signal can separate paths that are more than 30 cm away in the CIR. In this scenario, we can clearly identify at least four paths in the CIR and match these paths at different temperatures. Thus, we can measure the length of all these paths in one frame data at the same time.

We treat the problem as a continuous integral problem in Section 4 which is accurate yet hard to verify, since as far as we know, there is no existing COTS sensor that can provide air temperature distribution ground truth with such high resolution. Besides, in real-world, we may care more about the temperature in some specific cells, *e.g.*each seat in a car or in a conference room. The difference is that each cell is big, the time of sound signal traveling in it is no longer the same and the problem becomes a discrete problem. Assume that each cell in the sensing environment has a different temperature of T_i. In this case, the line integral in Eq. (12) changes to a weighted summation:

$$\tau^L - \tau_0^L = -\frac{0.606}{v_0^2} \sum_i w_i^L (T_i - T_0), \tag{13}$$

where the weights w_i^L are the length of the given path L passing through the region of cell i. When we have measurements on multiple paths, we can represent the ToF as a vector $\boldsymbol{\tau}$ and the temperature in different cells as a vector $\boldsymbol{T}$. The relationship between temperature and the ToF can be written as:

$$\boldsymbol{\tau} - \boldsymbol{\tau_0} = -\frac{0.606}{v_0^2} \boldsymbol{W}(\boldsymbol{T} - T_0), \tag{14}$$

where the weights $\boldsymbol{W}$ is an $m \times n$ matrix with each entry w_i^L, $1 \leq L \leq m, 1 \leq i \leq s$, representing the length of a given path L passing through the region of cell i, when we have n cells and m paths. We can then determine $\boldsymbol{T}$ by

$$\begin{aligned} \boldsymbol{T} &= -\frac{v_0^2}{0.606}\boldsymbol{W^g}(\boldsymbol{\tau} - \boldsymbol{\tau_0}) + T_0, \\ &= \underbrace{-\frac{v_0^2}{0.606}\boldsymbol{W^g}}_{coefficient}\ \boldsymbol{\tau} + \underbrace{\frac{v_0^2}{0.606}\boldsymbol{W^g}\boldsymbol{\tau_0} + T_0}_{intercept}, \end{aligned} \tag{15}$$

where $\boldsymbol{W^g}$ is the generalized inverse of $\boldsymbol{W}$. As we can observe from Fig. 1(a), different paths pass through the cells, *i.e.*, the four seats, in different ways. Therefore, they have different weights of w_i^L. If we know the weights, we can directly get temperature value in each cell. However, it's hard to accurately measure the length of all those reflection paths pass through each cell, we need a training stage to determine the weights w_i^L of each path. We solve this linear regression problem by the least absolute shrinkage and selection operator (LASSO) method or Ridge regression depending on the scenarios. In the training stage, we collect the ground truth temperature $\boldsymbol{T_g}$ from sensors on each cell and the ToF measurements $\boldsymbol{\tau}_m$ from our system. We apply a Kalman Filter to smooth the distance measurements before solving the linear regression problem. The weights $\boldsymbol{W}$ and all the other parameters ($\boldsymbol{\tau_0}$ and T_0) are constants when both Device A and B are fixed. Therefore, we only need to perform the training process once to determine these weights by mounting temperature sensors on each seat during the car manufacture process.

Although using multipaths to reconstruct the temperature distribution seems quite different from the continuous scenario, they are actually the same in the basic principle: analyzing different paths that acoustic signal passes and estimating the temperature in different region through sound speed. And when the number of paths are sufficient and the cell is small enough, the resolution of the discrete problem can match the continuous one. Besides, this solution can also be extended to 3-D scenarios.

5.2 Discussion

- **Number of available paths.** Lack of usable paths will make the problem an under-determined problem. Fortunately, multipaths in indoor environments are often rich enough to support our solution, *e.g.*we use a 4-mic array as Device A in Fig. 1(a) to measure ToF and can get at least $m = 4 \times 4 = 16$ paths. Thus, the number of paths is much larger than the number of cells and the linear equations are often over-determined.
- **In presence of human or obstacles.** If there are human or other obstacles in the environments after the calibration, they may block some of the paths and cause CIR fluctuation when they are moving around measurement paths. This will not affect the overall performance of our system since we can still leverage the unchanged paths in the environment. Multiple reflectors are helpful for our solution, because different signal paths may be more likely to go through different cells and contain more information that can be captured at the same time.
- **Acoustic devices.** Our solution can use widely deployed sound-devices in the environment, including TV sets, voice assistants, car speakers, and other smart-home appliances. We do not require the device to be able to play and record sound signals at the same time. Even if the device can only record sound, it can contribute to the number of sound paths given the location of it is known (as we do in Section 4). Our solution can utilize mobile phones for measurements. However, in general, mobile phones do not have fixed locations and they are not suitable for long-term sensing tasks [43].

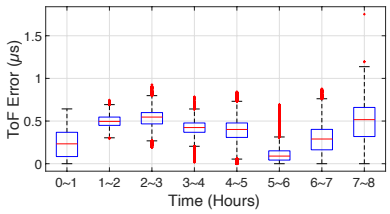

Fig. 10. Long-term ToF measurement result.

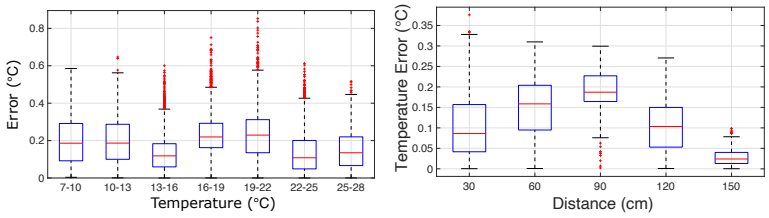

(a) Temperature measurement accuracy

(b) Temperature measurement accuracy at different distances

Fig. 11. Temperature sensing evaluations.

6 EVALUATIONS

6.1 Implementation

We have implemented VECTOR across different platforms including iOS, Android, and desktop operation systems. We have developed Android and iOS standalone applications that perform the signal processing and temperature estimating in real-time. For PCs or Raspberry Pi, we develop standalone Python version to do the same processing and a MATLAB server program to receive, visualize and process data from resource extremely limited devices. VECTOR operates at a central frequency of 19 kHz, occupies a bandwidth of 4 kHz (with $N_{zc} = 163$), and uses a frame length of 40 ms if not specified. The devices with different operating systems are compatible with each other if we use the same parameters for signal transmitting. For temperature sensing evaluations, we use two smartphones (two Samsung Galaxy S7 or two iPhone 6s) to estimate the temperature. For temperature distribution evaluation, we use smartphones and Raspberry Pis equipped with 4-microphones array to increase the receiving channel and get the measurement. To collect the data and analyze the result, we playback and record sound data simultaneously on the mobile phones/Raspberry Pis and transmit the recorded data to MATLAB via network in real-time. The temperature sensors are mounted on Raspberry Pi and the temperature ground truth is transmitted to the same PC. The PC records the timestamps of the two types of data by the time the socket package arrives and use the timestamps to synchronize to types of data, the network delay is usually shorter than the frame duration (40 ms) and is negligible.

6.2 Evaluation on ToF Measurement

VECTOR can stably measure the ToF for distributed devices with an average error of 0.371 μs *for 8 consecutive hours.* As VECTOR determines temperature through ToF measurement, we evaluate the ToF accuracy in an indoor environment with two identical smartphones (Samsung S7). We collect the temperature ground truth with BME280 temperature sensor, who has a temperature resolution of 0.01°C and an accuracy of 0.5°C [42] and the distance between two phones is fixed to 50 cm using a vernier. We calibrate the distance with the temperature sensor and keep the temperature of the room stable during the experiments. We then turn on VECTOR to continuously collect the ToF result for 8 hours. Fig. 10 shows the result of the ToF measurements within each hour, it shows that the result does not experience degradation along with time. The error variation between hours is mainly caused by the small temperature fluctuation, which is within 1°C during the experiments (between 21.6°C and 22.4°C). The average and 75th percentile errors for the 8 hours' measurements are 0.371 and 0.509 μs respectively. Our clock drift is orders of magnitude smaller than existing systems, *e.g.*, around 7 μs drift within ten minutes.

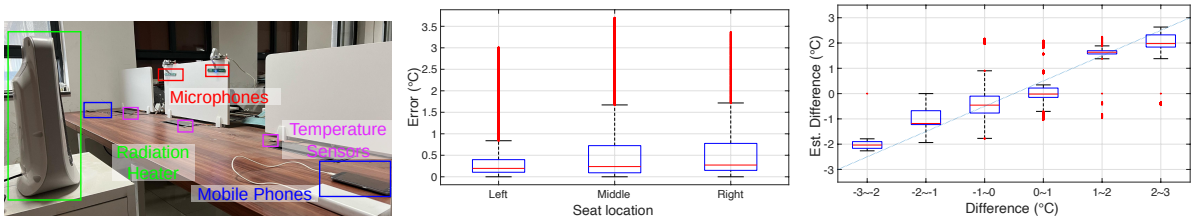

(a) Experiment setting on a table. (b) Seat temperature errors at different seats. (c) Seat temperature difference to the mean temperature of all seats.

Fig. 12. Temperature distribution estimating in a table.

6.3 Evaluation on Temperature Sensing

VECTOR achieves an average temperature error of less than $0.25^\circ C$ *in different static environments when compared with commercial temperature sensors.* To evaluate the temperature sensing capability of VECTOR, we place two Samsung S7 at a fixed distance on a table and measure the temperature along the LOS path. If not specified, we keep the doors and windows of the room closed and avoid any human perceivable air flows in the testing area. Fig. 11(a) shows the error distribution of VECTOR, where the ground truth is provided by a BME280 sensor. We repeat the experiments for more than 6,000 times in a period of three months by restarting VECTOR in different indoor environments, including labs, meeting rooms, and apartments with room temperatures in the range of $7 \sim 28^\circ$C. The average temperature error of VECTOR is smaller than 0.25°C and the maximum error is less than 0.9°C under different room temperatures. Fig. 11(b) shows that VECTOR can reliably measure the temperature when the devices are separated by 30 *cm* to 150 *cm* with room temperatures of $14 \sim 16^\circ$C.

6.4 Evaluation on Temperature Distribution Estimating

6.4.1 VECTOR achieves an average temperature error of $0.48^\circ C$ *for three seats along a table with four distributed devices (two transmitters and two receivers).* In this experiment, we use four separated devices to reconstruct the temperature distribution for three seats along the same table. Fig. 12(a) shows the deployment of this experiment, we use two mobile phones as transmitters, two microphone arrays as receivers and three BME280 sensors as ground truth. For each array, we use two microphones and we can get $2 \times 2 = 4$ LOS paths. We create temperature difference with a radiation heater and heat one seat a time, we collect the temperature and distance data for 66 minutes in total. In this experiment, we shuffle the data, train the linear model with random selected 1/10 of the data, and validate with the rest of the data. We repeat this process for 10 times for cross-validation and put the result together. We solve the linear function with Ridge Regression because the number of parameters is only slight more than the number of targets. The temperature range is $15.8^\circ\text{C} \sim 23.4^\circ$C, consisting of normal indoor temperature ($16 \sim 18^\circ$C) and heated temperature ($> 20^\circ$C). Fig. 12(b) shows the temperature result for three seats, VECTOR achieves an average temperature errors of 0.48°C. Fig. 12(c) shows the temperature difference between each seat and the average temperature ($T_i - \sum_i\{T_i\}/4$) where the average error for temperature difference is 0.43°C. Compared with synchronized devices, separated COTS acoustic devices are cheaper in price and worse in frequency offset. This experiment indicates that VECTOR can work with different kinds of device combinations.

6.4.2 VECTOR achieves an average temperature error of $0.44^\circ C$ *for temperature reconstruction of four seats in two different cars with one pair of transceivers.* In this experiment, we use longer frame with length of 7680 samples (160 *ms*) to increase the unambiguous range to 13.6 meters and capture reflection paths with longer distances. We mount VECTOR and four BME280 sensors on two different empty cars shown in Fig. 13 and collect the

(a) Car 1. (b) Car 2. (c) Experiment devices setting in car 1.

Fig. 13. Cars used in experiments and devices settings.

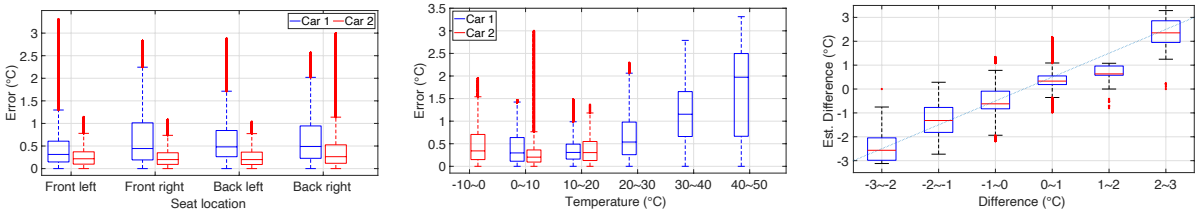

(a) Temperature errors at different seats. (b) Seat temperature errors at different temperature intervals. (c) Seat temperature difference to the mean temperature at all seats.

Fig. 14. Temperature distribution estimating in cars.

distance and temperature data. For distance data, we choose the reflection peaks with height higher than 85% of LOS peak to calculate the distance as feature candidates. For car 1, we collect the data for nine days in a period of thirteen days with a total duration of 25 hours; and for car 2, we collect the data for seven days in a period of eleven days with a total duration of 17 hours. Within each day, we collect data for at least two hours in different time periods including noon, afternoon, and night and under different weather conditions including sunny, cloudy, rainy and snowy. We cover different parts of the car to create temperature differences among seats in sunny days. The temperature range for car 1 and car 2 are $8.1°C \sim 46.2°C$ and $-1.9°C \sim 11.9°C$, respectively. Although the device position settings are similar in the two cars, due to the difference of structure and interior decoration, the reflection patterns are largely different which proves that our algorithm can generalize in different reflection conditions. Fig. 13(c) shows the device setting in car 1. We use data from three randomly picked days (*e.g.*, day 1, 3, 4) to train the paths' weight $\boldsymbol{W}$ and validate with data from the rest days (*e.g.*, day 2, 5, 6, 7, 8, 9), we repeat this process for ten times for cross validation and record all the errors as the result. Fig. 14(a) shows the temperature error for four seats derived by LASSO algorithm and Fig. 14(b) shows the temperature error distribution in different temperature interval. We observe that VECTOR achieves an average error of $0.59°C$ for car 1 and $0.29°C$ for car 2, and achieves total mean errors of $0.44°C$. The estimation error increases to around $2°C$ at high temperatures. This is possibly due to the mobile phone is overheated when temperature is higher than $30°C$. Fig. 14(c) shows the temperature difference between each seat and the average temperature, $T_i - \sum_i\{T_i\}/4$. When temperatures on seats are differed by $-3 \sim 3°C$, VECTOR can measure temperature difference with an average error of $0.57°C$. This indicates that VECTOR can reliably detect the temperature differences within a car.

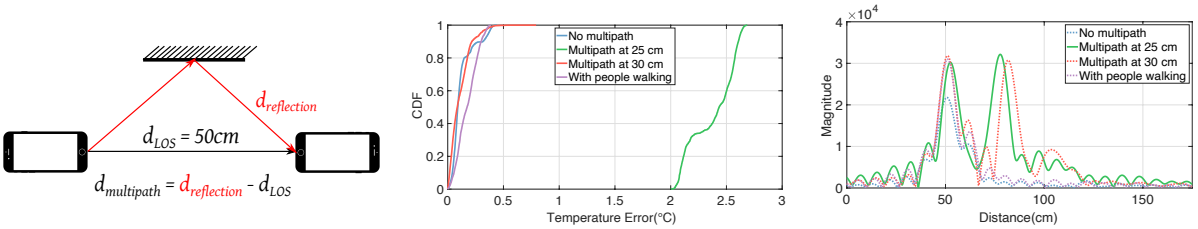

(a) Device settings in multipaths experiment.

(b) Experiment result for different distances and types of multipaths.

(c) Influence of different distances and types of multipaths on CIR.

Fig. 15. Experiments on multipaths.

6.5 Evaluation on Robustness

6.5.1 VECTOR is robust to multipaths with distance ≥ 30 cm away from LOS.. We run VECTOR in presence of multipaths to evaluate the impact of multipaths. We place two mobile phones at a distance of 50 cm on a table and create multipath conditions of four different types: no multipath, at 25cm, at 30cm by placing a metal plate, and a people walking around 50 cm away from LOS. The multipaths distance is calculated as $d_{reflection} - d_{los}$ as shown in Fig. 15(a). We place the steel plate after we calibrate the system because our calibration process would cancel the impact of the multipath, including reflections from the surface of the table as well as the structure-borne sound of the table and the devices. The 75 percentile temperature errors of these four types of multipath conditions are 0.13°C, 2.56°C, 0.16°C, and 0.25°C, as shown in Fig. 15(b). The detailed correlation peaks of multipath are shown in Fig. 15(c). Multipaths will create new peaks in the CIR whose positions are related to the distance, if the distance is longer than 30 cm, the new peaks will not affect the LOS peak. If the distance is less than 30 cm, *e.g.*, 25 cm, the two peaks merge together and the ToF result is largely affected. The moving obstacles slightly affect the result due to the complex reflection patterns in certain frames even if they are 50 cm away from the LOS path. The range resolution can be improved by using longer frames with wider bandwidth and in-practice we can detect and remove paths that have close obstacles.

6.5.2 VECTOR is robust to different device orientations. We place the two mobile phones in different orientations shown as Fig. 16(a) to reveal the influence of devices' relative orientation. The distance between devices is around 50 *cm*. Since the propagation distances between devices in this scenario are hard to measure, we perform an one-time calibration with one frame of ToF and temperature sensor's reading. After the one-time calibration, as long the devices are fixed, no extra process is needed. This experiment is conduct in indoor environment with temperature around 23 ∼ 25°C. We collect the ground truth with BME280 temperature sensors. In every orientation setting, we collect the temperature data for 10 minutes for comparison. Fig. 16(b) shows the result of this experiment and VECTOR is robust to different device orientation setting. While the propagation of ultrasound is more directional than audible sound, it could still provide an acceptable SNR to support our application even in the 90° orientation setting. This experiment also demonstrates that VECTOR does not have strict device deployment requirements, *e.g.*, devices have to face each other.

6.5.3 VECTOR is robust to audible noise and high frequency continuous wave noise. We expose VECTOR under different noises to analyze the impact of noise. We run VECTOR under these noises for a duration of 10 minutes. These noises exist in both calibration and processing stage. The audible noise's sound level is measured with a sound level meter in unit *dBA*. We play the high-frequency noises (continuous wave signal at 19 *kHz* and ZC sequence in the same frequency band with different parameters) with another mobile phone and the level of

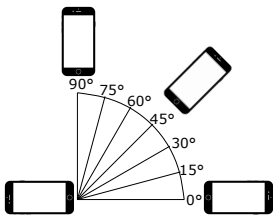

(a) Devices in different orientation setting.

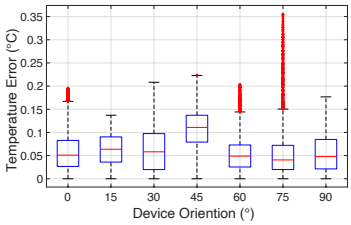

(b) Experiment result for different orientation of devices.

Fig. 16. Experiments on device orientation.

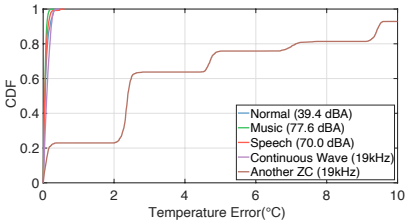

Fig. 17. Temperature results' under different kind of noises.

them cannot be measured by the sound level meter. Fig. 17 shows the result of this experiment. For the five different situations (normal, music, speech, continuous wave, and another ZC), VECTOR achieves a 75 percentile temperature errors of 0.11, 0.07, 0.08, 0.17, and 4.87°C. According to our observation, high frequency continuous wave will add an constant value on the CIR's magnitude and the influence can be canceled by the ToF calculation process. Moreover, aother ZC sequence will cause some noisy peaks on the CIR and affect the phase and position of the LOS peak. This experiment shows that VECTOR can stay robust under audible environmental noises and high-frequency continuous wave noise. It's noted that if the noise interference's level is too high and makes the signal clipped on the recording side, the result will be greatly affected no matter what frequency band the noise uses.

6.6 Enhancements Compared with Traditional Sensors

6.6.1 VECTOR is sensitive enough to recognize different types of heat sources with an accuracy higher than 90%. We collected temperature measurements for three different scenarios: normal room without heating, heated by air conditioners and radiator heater, with monitoring duration of 166.7, 221.4, and 292.0 minutes, respectively. We observe that the normal indoor environment has a small temperature standard deviation of 0.10°C within a time window of 30 seconds, but air conditioners and heaters introduce higher variations of 0.28°C and 0.18°C. While both are heating devices, the temperature variation patterns of the air conditioner and the heater are also different. Fig. 18 shows the amplitude of low-frequency and high-frequency variation in different environments obtained by performing FFT over time windows with a length of 100 seconds. We observe that different types of heating devices are clearly separable using the spectrum of temperature variations. With a decision tree algorithm based on the spectrum features, we can recognize the normal environment, the air conditioner, and the radiator heater with an accuracy of 96.0%, 91.8%, and 92.8%, respectively.

6.6.2 VECTOR detects environment changes by 18.39 seconds faster than the traditional temperature sensors on average. We use a commercial heating pad to heat the air and use a BME280 sensor and VECTOR to measure the temperature changes. We first put VECTOR and a BME280 sensor in the same normal indoor environment and then we start the heating pad to heat the air around the sensors. The heating pad is connected to a controlling module provided by the manufacturer and will periodically turn on and off to match a target temperature. The data for VECTOR and BME280 sensor are synchronized and we capture the ground truth of on-off events using a camera. We repeat this experiment for 20 times and each experiment lasts for half an hour (including heating and cooling down). Fig. 19(a) shows the time that VECTOR and BME280 sensor first detect the switch off (reach the temperature measurement's first turning point). The average detection time for VECTOR and BME280 sensor are 2.56 *s* and 20.95 *s* respectively. Fig. 19(b) shows an example of the heating process, where we can clearly observe

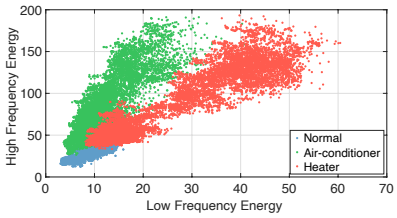

Fig. 18. Frequency component of temperature variations for different heating source.

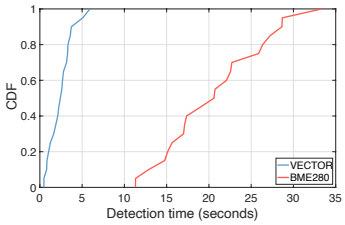

(a) Detection time for VECTOR and BME280 when they first detect the heating switch off.

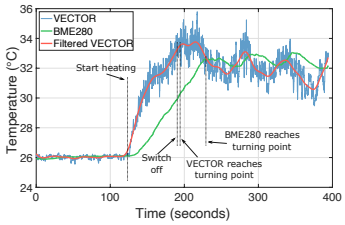

(b) An example of temperature fast response experiments.

Fig. 19. Temperature fast response evaluations.

the lag of traditional BME280 sensors. We have experimented on other traditional temperature sensors, such as BME380, and the results are similar. The timely feedback can largely increase the performance of temperature control system.

6.7 System Performance and User Study

6.7.1 VECTOR can process the audio signal in real-time on commercial iOS, Android mobile phones and Raspberry Pi. We measure the signal processing time for one frame acoustic signal (40 *ms*) on different platform including iPhone 6S, Samsung S7, and Raspberry Pi 3B+. Signal processing includes signal segmenting the raw signal, demodulation, phase calculation, and temperature estimation. Table 1 shows the processing time for different platforms. VECTOR on iOS is implemented with the vDSP acceleration framework and takes a negligible 0.494 *ms* processing delay on average. We use Java Native Interface (JNI) on Android mixed with C for core functions to process the signal. The implementation on Android can meet the real-time timing requirement but has an order of magnitude delay than the vDSP version. Our system can also process the data in real-time on resource-limited device like Raspberry Pi using Numpy in Python. In general, our design is light-weighted and can be deployed on various hardware platforms used in smart-home devices.

6.7.2 VECTOR's transmitting signal can be barely heard by users. We invite 30 volunteers (including 18 males and 12 females) from age 22 to 49 to test the audibility of the transmitting signal on their own mobile devices or earphones with maximum volume. Table 2 shows the result of this experiment. Three out of 18 male volunteers can hear the signal and for female volunteers, one out of 12 can hear it. Furthermore, the volunteers who can hear it described that the sound can only be heard with concentration. Therefore, the sound signal played by our system would not affect people's daily activities. We can also reduce the sound level or use better playing devices that support higher frequency bands to make our signal fully inaudible.

Table 1. Processing time on different devices.

Device	Signal processing (*ms*)
iPhone 6S	0.494 ± 0.476
Samsung S7	10.841 ± 3.683
Raspberry Pi 3B+	16.731 ± 2.154

Table 2. Audibility to users.

Gender	Audible/total number
Male	3/18
Female	1/12

7 LIMITATIONS AND DISCUSSIONS

There are five limitations in current design of VECTOR as listed below.

Calibration/training stage. For temperature sensing, the calibration stage measures the initial distance between two or more devices. The distances sometimes are hard to measure when the devices are not facing each other. Therefore, our approach is fixing the devices, getting the distance measurements and calculating the actual distance with an extra temperature sensor's reading. This process is simple and only takes few seconds to conduct during the deployment phase. We have one assumption about this stage that the environment is under full control which means there is no interference including high frequency wideband noise and/or moving obstacles close to the LOS path. When it comes to temperature distribution estimation with reflections, we have to create temperature difference across cells to learn the reflection pattern of the environment in the training stage. This can be done in the manufacture stage of the car or deployment stage in the room with temperature sensor and heater. That being said, it is still laborsome to create different temperature distributions, *e.g.*, in our evaluations, we leverage sun's heat and cover the car to create temperature difference between seats across days. Estimating the reflection pattern efficiently during the calibration stage is still challenging.

Multipath and other interference. As shown in Section 6.5, the close multipath (static or moving) and high-frequency wideband signal will affect the performance and this is inevitable in home/car setting. There might be two approaches to solve this problem. The first possible solution is using deep learning method to cancel the impact of multipaths and noises as in [41]. However, existing deep learning systems only solve the distance with a single path for static obstacles. The second possible solution is to detect these interference and only perform temperature estimation when there is no interference or with unaffected paths. Whether the paths are affected can be detected by the shape of CIR, SNR, and distributions of the distance of the given path.

Parameters. The reflection weight $\boldsymbol{W}$ in Equation 15 are tightly coupled with the environment. According to our theoretical model, the weight $\boldsymbol{W}$ indicates how one acoustic signal path (LOS or reflection path) propagates through each cell and it's highly related to the environment, which means we need to re-estimate the weight when transferring to a new environment.

Impact of air-flow and wind. We conduct our evaluations avoiding strong air-flow and wind because they will affect the sound speed and ToF measurement. This is necessary in the heat source detection experiment, because we want to demonstrate that VECTOR can recognize heat source with pure temperature changing patterns instead of air-flow caused patterns. According to our observation, the impact of wind on ToF changes is largely different from temperature caused changes and physical/theoretical model can be helpful to analyze this phenomenon and cancel their impact.

Temperature distribution estimation with multipath. To estimate the temperature distribution with multipath, we solve the relationship between paths and cells with linear regression based on theoretical analysis. Although the interpretability of this approach is good, the accuracy of the temperature estimation could be furthre improved. With the mean errors being acceptable (around 0.5°C), the variance of the errors is very large (up to $2 \sim 3$°C), which might be caused by insufficient data and outliers. Powerful deep learning model may help to attend to these interference using complex CIR or distances for different paths as input without going through every possible situation.

8 RELATED WORK

Recent works related to VECTOR are in the following three categories.

Temperature sensors. Nowadays, temperature sensors widely used in daily lives are generally in two types: physical attributes based sensors [44–47] and optical/infrared sensors [48]. The first type of sensors leverage temperature-sensitive physical parameters of materials, including resistance [47], fluid expand [44] and *etc.*. In this case, sensing materials have to be well-heated to exhibit these property and the response delay could be large, *e.g.*, the mercurial thermometer takes minutes to return the right body temperature. Recently, Yang *et al.* proposed a new polydimethylsiloxane/carbon nanotubes based temperature sensor to provide fast and

accurate body temperature [49]. Caselli *et al.* designed an integrated temperature sensor for food monitoring with low power consumption and tiny size [50]. Breda *et al.* proposed to infer the ambient temperature with the battery temperature sensor of mobile devices [51]. To improve performance from multiple sensors' readings, [52] combines 9 sensors with improved linear regression to predict the temperature of CPU, and [53] performs deep learning based data fusion to monitor the air temperature distribution of greenhouse. For optical/infrared thermometers, they detect thermal radiation/black body radiation from objects and infer the temperature [48]. They are fast, contactless, and can infer the temperature from different objects at the same time. Thus, infrared thermometers are widely used in medical and industry applications [54–56]. Thermal comfort for occupants and operational characteristics of residual air-conditioners can be inferred from optical temperature sensors [57, 58]. However, optical sensors are often expensive [11] and need LOS path to the target [56], *e.g.*, even a thin cover could block the heat emission from detection. Acoustic based temperature sensing has advantages of fast response time, temperature distribution estimation, and low costs compared with these specialized temperature sensors.

Wireless temperature monitoring. Wireless temperature monitoring either use radio signals or acoustic signals for temperature monitoring. RFIDs are popular for wireless temperature sensing due to their battery-free and long-range coverage features [13, 14, 59, 60]. However, each RFID can only measure the temperature at a single location as traditional temperature sensors. Although the price for a single tag is low, the cost of RFID readers are high compared with acoustic devices. Ha *et al.* leveraged WiFi signal strength to contactless classify body temperature, and they can only get a coarse-grained 3-classes result (cool, normal, and warm [61]). ThermoWave interrogates the cholesteryl materials with millimeter wave and leverage the frequency domain feature of the bounce back signal to get the single-point temperature and further builds a learning-based model to infer the temperature distribution [15]. For acoustic-based sensing, Acute uses mobile phones to transmit and receive acoustic signal on the same device to perform temperature measurement [12, 62]. However, due to the short distance between speakers and microphones on the same device, Acute only measures temperature around the device and can only infer coarse-grained room-level temperature distribution using interpolation on single-point measurements. Guided wave based temperature monitoring model is built for hot section of aeroengines monitoring with high precision ultrasound sensors [63], however it focuses on the building the velocity model and simulation and did not provide temperature accuracy result. AcousticThermo transmits and receives acoustic pulse signal from a synchronized device and leverage the reflection distance from nearby wall to calculate the changes in sound speed and estimate the temperature in high accuracy (0.2°C) [64]. However, AcousticThermo requires specified ultrasound sensors operating at 40 kHz, which is not supported by most COTS devices, and their precision is coupled with the sampling rate because they do not leverage the phase information. Furthermore, AcousticThermo is unable to estimate the temperature distribution because they need the device deployed close to a wall and estimate the temperature with single path. Specialized industry acoustic sensors have been used for temperature measurements in inaccessible areas, *e.g.*, the temperature in a reaction chamber [65, 66]. With multiple transmitters and receivers, it is also possible to rebuild the temperature distribution in a given region [67, 68]. However, most of existing systems use specialized and synchronized transceivers so that they cannot be widely deployed in smart home and environment monitoring scenarios.

Acoustic signal calibration. Acoustic sensing system have been widely used for gesture recognition [69–71], vital sign monitoring [72–74], and localization [75, 76]. Acoustic ranging systems [36, 77, 78] measures the ToF of sound signals in a similar way as in VECTOR. These systems use phase-based approach to achieve millimeter-level tracking accuracy [33, 35, 79, 80]. However, when applied to physically distributed devices, they require user intervention for calibration, when the devices start playing/recording the sound. Such calibration process often requires devices to be placed at a fixed location or move along a given trajectory, to estimate the unknown clock offset [33, 35]. Compared with these systems, VECTOR provides long-term stable ToF measurements without user intervention. Our system only needs a single calibration under a known temperature during the deployment phase.

9 CONCLUSIONS

In this paper, we developed VECTOR, a temperature-field monitoring system, that achieves high temperature sensing accuracy using commercial sound playing/recording devices. Our system can provide a timely feedback and temperature distributions over space for the future temperature control systems. We provide two solutions for temperature distribution measurement: for densely deployed devices, we propose a dRadon algorithm to reconstruct a fine-grained temperature distribution; for systems with a small number of devices, we ally with multipaths and get a coarse-grained temperature distribution in different cells. We believe that our system will be useful in many real-life temperature monitoring/control systems.

ACKNOWLEDGMENTS

We would like to thank our anonymous reviewers for their valuable comments. This work is partially supported by National Natural Science Foundation of China under Numbers 61872173, 61902177, 61972254, 61832005, 61872178 and 62102006, Natural Science Foundation of Jiangsu Province of China under number BK20190298 and Collaborative Innovation Center of Novel Software Technology.

REFERENCES

[1] Yanghui Ou, Xifu Wang, and Jingyun Liu. Warehouse multipoint temperature and humidity monitoring system design based on kingview. *AIP Conference Proceedings*, 1834(1):040009, 2017.
[2] A. Pedrini, F.S. Westphal, and R. Lamberts. A methodology for building energy modelling and calibration in warm climates. *Building and Environment*, 37(8):903–912, 2002.
[3] Doaa M. Atia and Hanaa T. El-madany. Analysis and design of greenhouse temperature control using adaptive neuro-fuzzy inference system. *Journal of Electrical Systems and Information Technology*, 4(1):34–48, 2017.
[4] Proper storage temperatures for usda commodities. https://www.cde.ca.gov/ls/nu/fd/mb00404.asp, 2021.
[5] CK Chau, EY Tu, D W T Chan, and J Burnett. Estimating the total exposure to air pollutants for different population age groups in hong kong. *Environment international*, 27(8):617—630, March 2002.
[6] Klepeis NE, Nelson WC, Ott WR, Robinson JP, Tsang AM, Switzer P, Behar JV, Hern SC, and Engelmann WH. National Human Activity Pattern Survey (NHAPS): A resource for assessing exposure to environmental pollutants. *J Expo Anal Environ Epidemiol*, 11(3):231–252, 2001.
[7] Catalin Teodosiu, Raluca Hohota, Gilles Rusaouën, and Monika Woloszyn. Numerical prediction of indoor air humidity and its effect on indoor environment. *Building and Environment*, 38(5):655–664, 2003.
[8] Air conditioning use emerges as one of the key drivers of global electricity-demand growth. https://www.iea.org/news/air-conditioning-use-emerges-as-one-of-the-key-drivers-of-global-electricity-demand-growth, 2018.
[9] Roberto Z. Freire, Gustavo H.C. Oliveira, and Nathan Mendes. Predictive controllers for thermal comfort optimization and energy savings. *Energy and Buildings*, 40(7):1353–1365, 2008.
[10] Siyu Wu and Jian-Qiao Sun. A physics-based linear parametric model of room temperature in office buildings. *Building and Environment*, 50:1–9, 2012.
[11] FLIR E5-XT infraed camera. https://www.flir.com/products/e5-xt/, 2015.
[12] Chao Cai, Zhe Chen, Henglin Pu, Liyuan Ye, Menglan Hu, and Jun Luo. AcuTe: Acoustic thermometer empowered by a single smartphone. In *Proceedings of ACM SenSys*, 2020.
[13] Xingyu Chen, Jia Liu, Fu Xiao, Shigang Chen, and Lijun Chen. Thermotag: Item-level temperature sensing with a passive rfid tag. In *Proceedings of ACM MobiSys*, 2021.
[14] Swadhin Pradhan and Lili Qiu. Rtsense: Passive rfid based temperature sensing. In *Proceedings of ACM SenSys*, 2020.
[15] Baicheng Chen, Huining Li, Zhengxiong Li, Xingyu Chen, Chenhan Xu, and Wenyao Xu. Thermowave: A new paradigm of wireless passive temperature monitoring via mmwave sensing. In *Proceedings of ACM MobiCom*, 2020.
[16] Gengsheng Lawrence Zeng. *Medical image reconstruction: a conceptual tutorial.* Springer, 2010.
[17] Grand View Research. *Automotive Electronics Market Size, Share & Trends Analysis Report By Component (Electronic Control Unit, Sensors, Current Carrying Devices), By Application, By Sales Channel, By Region, And Segment Forecasts, 2021 - 2028.* Grand View Research, San Francisco, CA, 2021.
[18] Mordor Intelligence. *Automotive Wiring Harness Market - Growth, Trends, COVID-19 Impact, and Forecasts (2022 - 2027).* Mordor Intelligence, Hyderabad, Telangana, India, 2021.

[19] Arman Shehabi, Dale Sartor Sarah Smith, Richard Brown, Magnus Herrlin, Jonathan Koomey, Eric Masanet, Nathaniel Horner, Inês Azevedo, and William Lintner. *United States Data Center Energy Usage Report.* Lawrence Berkeley National Lab (LBNL), Berkeley, CA, 2016.
[20] Infocomm Media Development Authority. *Singapore announces a proof-of-concept for the world's first Tropical Data Centre (TDC).* https://www.imda.gov.sg/news-and-events/impact-news/2016/06/tropical-revolution-for-data-centres, 2013.
[21] Rongrong Wang, Duc Van Le, Rui Tan, Yew-Wah Wong, and Yonggang Wen. Real-time cooling power attribution for co-located data center rooms with distinct temperatures. In *Proceedings of ACM BuildSys*, 2020.
[22] Victor-Alexandru Pădurean, Andrei-Alexandru Cristea, and Marcel Antal. Heat reuse models for liquid cooled data centers integrated with district heating. In *Proceedings of ACM BuildSys*, 2021.
[23] Marcel Antal, Tudor Cioara, Ionut Anghel, Claudia Antal, and Ioan Salomie. Flexibility management of data centers to provide energy services in the smart grid. In *Proceedings of ACM e-Energy*, 2021.
[24] Optimize airflow and hvac for data center. https://www.energystar.gov/products/data_centers/optimize_airflow_hvac, 2022.
[25] Eronini I. Umez-Eronini. *System Dynamics and Control.* CL-Engineering, first edition edition, 1998.
[26] Joe Brown, Jonathan Chambers, Alessandro Abate, and Alex Rogers. Smite: Using smart meters to infer the thermal efficiency of residential homes. In *Proceedings of ACM BuildSys*, 2020.
[27] Jonathan D. Chambers and Tadj Oreszczyn. Deconstruct: A scalable method of as-built heat power loss coefficient inference for uk dwellings using smart meter data. *Energy and Buildings*, 183:443–453, 2019.
[28] Google nest thermostat. https://www.nest-thermostat.com/, 2022.
[29] Nadine von Frankenberg, Vivian Loftness, and Bernd Bruegge. I want it that way: Thermal desirability in shared spaces. In *Proceedings of ACM BuildSys*, 2021.
[30] Elvin Vindel, Mario Bergés, Burcu Akinci, and Olga Kavvada. Demand flexibility potential model for multi-zone commercial buildings using internal hvac system states. In *Proceedings of ACM BuildSys*, 2021.
[31] Srinarayana Nagarathinam, Arunchandar Vasan, Venkatesh Sarangan, Rajesh Jayaprakash, and Anand Sivasubramaniam. Good set-points make good neighbors: User seating and temperature control in uberized workspaces. In *Proceedings of ACM BuildSys*, 2018.
[32] Lawrence E Kinsler, Austin R Frey, Alan B Coppens, and James V Sanders. *Fundamentals of Acoustics.* Wiley, fourth edition edition, 2000.
[33] Anran Wang and Shyamnath Gollakota. MilliSonic: Pushing the limits of acoustic motion tracking. In *Proceedings of ACM CHI*, 2019.
[34] International Electrotechnical Commission. Digital audio interface – part1: General. IEC 60958-1, 2014.
[35] Wenguang Mao, Jian He, and Lili Qiu. CAT: High-precision acoustic motion tracking. In *Proceedings of ACM MobiCom*, 2016.
[36] Sangki Yun, Yi-Chao Chen, and Lili Qiu. Turning a mobile device into a mouse in the air. In *Proceedings of ACM MobiSys*, 2015.
[37] Branislav M Popovic. Generalized chirp-like polyphase sequences with optimum correlation properties. *IEEE Transactions on Information Theory*, 38(4):1406–1409, 1992.
[38] Ke Sun, Ting Zhao, Wei Wang, and Lei Xie. VSkin: Sensing touch gestures on surfaces of mobile devices using acoustic signals. In *Proceedings of ACM MobiCom*, 2018.
[39] Chunyi Peng, Guobin Shen, Yongguang Zhang, Yanlin Li, and Kun Tan. BeepBeep: A high accuracy acoustic ranging system using COTS mobile devices. In *Proceedings of ACM SenSys*, 2007.
[40] Wenguang Mao, Mei Wang, Wei Sun, Lili Qiu, Swadhin Pradhan, and Yi-Chao Chen. Rnn-based room scale hand motion tracking. In *Proceedings of ACM MobiCom*, 2019.
[41] Wenguang Mao, Wei Sun, Mei Wang, and Lili Qiu. Deeprange: Acoustic ranging via deep learning. *Proceedings of ACM IMWUT*, 2020.
[42] Bosch. BME280 combined humidity, pressure and temperature sensor, 2018.
[43] Noah Klugman, Meghan Clark, Pat Pannuto, and Prabal Dutta. Android resists liberation from its primary use case. In *Proceedings of ACM MobiCom*, 2018.
[44] Dario Camuffo and Chiara Bertolin. The earliest spirit-in-glass thermometer and a comparison between the earliest cet and italian observations. *Weather*, 67(8):206–209, 2012.
[45] Xun Gong, Xiaohe Tang, Yanjie Li, Minmin You Zude Lin, and Jingquan Liu. Investigation the minimum measurement points for calibration a high precision ntc thermistors in cryogenic field. In *Proceedings of IEEE NEMS*, pages 1088–1091, 2021.
[46] R. Walker. Recent advances in resistance thermometry readouts. In *NCSL International Workshop and Symposium*, 2010.
[47] R. Denos and C. H Sieverding. Assessment of the Cold-Wire Resistance Thermometer for High-Speed Turbomachinery Applications. *Journal of Turbomachinery*, 119(1):140–148, 01 1997.
[48] Tetsuya Jitsufuchi. Thermal infrared surveys for mapping surface temperature and sulfur dioxide plumes at sakurajima volcano (minamidake a-crater, showa crater) using the airborne hyperspectral scanner. In *Proceedings of IEEE IGARSS*, pages 715–718, 2013.
[49] Jingshuo Yang. Flexible temperature sensor based on pdms/cnt/ti3c2tx for physiological temperature monitoring. In *Proceedings of ACM ISAIMS*, 2021.
[50] Michele Caselli, Marco Ronchi, and Andrea Boni. An integrated low power temperature sensor for food monitoring applications. In *Proceedings of IEEE ISCAS*, 2021.

[51] Joseph Breda, Amee Trivedi, Chulabhaya Wijesundara, Phuthipong Bovornkeeratiroj, David Irwin, Prashant Shenoy, and Jay Taneja. Hot or not: Leveraging mobile devices for ubiquitous temperature sensing. In *Proceedings of ACM BuildSys*, 2019.
[52] Ning Wang and Jia-Yang Li. Efficient multi-channel thermal monitoring and temperature prediction based on improved linear regression. *IEEE Transactions on Instrumentation and Measurement*, 71:1–9, 2022.
[53] Sibo Xia, Xinyuan Nan, Xin Cai, and Xumeng Lu. Data fusion based wireless temperature monitoring system applied to intelligent greenhouse. *Computers and Electronics in Agriculture*, 192:106576, 2022.
[54] Desenclos JC Bitar D, Goubar A. International travels and fever screening during epidemics: a literature review on the effectiveness and potential use of non-contact infrared thermometers. *Euro Surveill*, 1(1):21, 02 2009.
[55] Shelley N Facente, Lauren A Hunter, Laura J Packel, Yi Li, Anna Harte, Guy Nicolette, Shana McDevitt, Maya Petersen, and Arthur L Reingold. Feasibility and effectiveness of daily temperature screening to detect COVID-19 in a prospective cohort at a large public university. *BMC Public Health*, 1(1):21, 09 2021.
[56] Racha Benarrait, Frederic Lamarque, Jeremy Terrien, Hani Al Hajjar, Muneeb Ullah Khan, and Andreas Dietzel. Optical power supply of a wireless temperature sensor for rotating machines monitoring purpose. In *Proceedings of IEEE I2MTC*, pages 1–6, 2021.
[57] Ashrant Aryal and Burcin Becerik-Gerber. Skin temperature extraction using facial landmark detection and thermal imaging for comfort assessment. In *Proceedings of ACM BuildSys*, 2019.
[58] Pandarasamy Arjunan, Gregory Dobler, Kyungmin Lee, Clayton Miller, Filip Biljecki, and Kameshwar Poolla. Operational characteristics of residential air conditioners with temporally granular remote thermographic imaging. In *Proceedings of ACM BuildSys*, 2021.
[59] A. Vaz, A. Ubarretxena, I. Zalbide, D. Pardo, H. Solar, A. Garcia-Alonso, and R. Berenguer. Full passive uhf tag with a temperature sensor suitable for human body temperature monitoring. *IEEE Transactions on Circuits and Systems II: Express Briefs*, 57(2):95–99, 2010.
[60] Jun Yin, Jun Yi, Man Kay Law, Yunxiao Ling, Man Chiu Lee, Kwok Ping Ng, Bo Gao, Howard Cam Luong, Amine Bermak, Mansun Chan, Wing-Hung Ki, Chi-Ying Tsui, and Matthew Ming-Fai Yuen. A system-on-chip epc gen-2 passive uhf rfid tag with embedded temperature sensor. In *Proceedings of IEEE ISSCC*, pages 308–309, 2010.
[61] Vincent Ha and Ani Nahapetian. Received wifi signal strength monitoring for contactless body temperature classification. In *Body Area Networks. Smart IoT and Big Data for Intelligent Health Management*, pages 112–125. Springer International Publishing, 2022.
[62] Chao Cai, Henglin Pu, Menglan Hu, Rong Zheng, and Jun Luo. SST: Software sonic thermometer on acoustic-enabled IoT devices. *IEEE Transactions on Mobile Computing*, 2020.
[63] Lawrence Yule, Bahareh Zaghari, Nicholas Harris, and Martyn Hill. Modelling and validation of a guided acoustic wave temperature monitoring system. *Sensors*, 21(21), 2021.
[64] Fusang Zhang, Kai Niu, Xiaolai Fu, and Beihong Jin. Acousticthermo: Temperature monitoring using acoustic pulse signal. In *Proceedings of IEEE MSN*, 2020.
[65] Wen-Yuan Tsai, Hsin-Chieh Chen, and Teh-Lu Liao. High accuracy ultrasonic air temperature measurement using multi-frequency continuous wave. *Sensors and Actuators A: Physical*, 132(2):526–532, 2006.
[66] YS Huang and Ming-Shing Young. An accurate ultrasonic distance measurement system with self temperature compensation. *Instrumentation Science and Technology*, 37(1):124–133, 2009.
[67] Xuehua Shen, Qingyu Xiong, Xin Shi, Kai Wang, Shan Liang, and Min Gao. Ultrasonic temperature distribution reconstruction for circular area based on markov radial basis approximation and singular value decomposition. *Ultrasonics*, 62:174–185, 2015.
[68] Ruixi Jia, Qingyu Xiong, Guangyu Xu, Kai Wang, and Shan Liang. A method for two-dimensional temperature field distribution reconstruction. *Applied Thermal Engineering*, 111:961–967, 2017.
[69] Rajalakshmi Nandakumar, Vikram Iyer, Desney Tan, and Shyamnath Gollakota. FingerIO: Using active sonar for fine-grained finger tracking. In *Proceedings of ACM CHI*, 2016.
[70] Wenjie Ruan, Quan Z Sheng, Lei Yang, Tao Gu, Peipei Xu, and Longfei Shangguan. AudioGest: Enabling fine-grained hand gesture detection by decoding echo signal. In *Proceedings of ACM Ubicomp*, 2016.
[71] Ke Sun, Wei Wang, Alex X. Liu, and Haipeng Dai. Depth aware finger tapping on virutal displays. In *Proceedings of ACM MobiSys*, 2018.
[72] Rajalakshmi Nandakumar, Shyamnath Gollakota, and Nathaniel Watson. Contactless sleep apnea detection on smartphones. In *Proceedings of ACM MobiSys*, 2015.
[73] Tianben Wang, Daqing Zhang, Yuanqing Zheng, Tao Gu, Xingshe Zhou, and Bernadette Dorizzi. C-FMCW based contactless respiration detection using acoustic signal. In *Proceedings of ACM UbiComp*, 2018.
[74] Anran Wang, Jacob E Sunshine, and Shyamnath Gollakota. Contactless infant monitoring using white noise. In *Proceedings of ACM MobiCom*, 2019.
[75] Bing Zhou, Mohammed Elbadry, Ruipeng Gao, and Fan Ye. BatMapper: Acoustic sensing based indoor floor plan construction using smartphones. In *Proceedings of ACM MobiSys*, 2017.
[76] Yu-Chih Tung and Kang G Shin. Echotag: Accurate infrastructure-free indoor location tagging with smartphones. In *Proceedings of ACM MobiCom*, 2015.
[77] Cheng Zhang, Qiuyue Xue, Anandghan Waghmare, Sumeet Jain, Yiming Pu, Sinan Hersek, Kent Lyons, Kenneth A Cunefare, Omer T Inan, and Gregory D Abowd. Soundtrak: Continuous 3D tracking of a finger using active acoustics. In *Proceedings of ACM UbiComp*,

2017.
[78] Zengbin Zhang, David Chu, Xiaomeng Chen, and Thomas Moscibroda. Swordfight: Enabling a new class of phone-to-phone action games on commodity phones. In *Proceedings of ACM MobiSys*, 2012.
[79] Yunting Zhang, Jiliang Wang, Weiyi Wang, Zhao Wang, and Yunhao Liu. Vernier: Accurate and fast acoustic motion tracking using mobile devices. In *Proceedings of IEEE INFOCOM*, 2018.
[80] Gaoshuai Cao, Kuang Yuan, Jie Xiong, Panlong Yang, Yubo Yan, Hao Zhou, and Xiang-Yang Li. Earphonetrack: Involving earphones into the ecosystem of acoustic motion tracking. In *Proceedings of ACM SenSys*, 2020.